Available online at www.sciencedirect.com

jmr&t Journal of Materials Research and Technology

journal homepage: www.elsevier.com/locate/jmrt

Original Article

Laser powder bed fusion parameters to produce high-density Ti–53%Nb alloy using irregularly shaped powder from hydride-dehydride (HDH) process

Jhoan Guzmán [a,b], *Rafael de Moura Nobre* [a], *Enzo R. Nunes* [a], *D.L. Bayerlein* [b,c], *R.B. Falcão* [b], *Edwin Sallica-Leva* [b], *João Batista Ferreira Neto* [d], *Henrique Rodrigues Oliveira* [e,f], *Victor Lira Chastinet* [e], *Fernando J.G. Landgraf* [a,*]

[a] *Department of Metallurgical and Materials Engineering (PMT), Polytechnic School of the University of São Paulo (EPUSP), Av. Professor Mello Moraes 2463, São Paulo, SP, Brazil*

[b] *Laboratory of Metallurgical Processes (LPM), Institute for Technological Research (IPT), Av. Prof. Almeida Prado 532, São Paulo, SP, Brazil*

[c] *Nuclear and Energy Research Institute (IPEN), São Paulo, SP, Brazil*

[d] *Brazilian Metallurgy and Mining Company (CBMM), Araxá, MG, Brazil*

[e] *SENAI Innovation Institute for Manufacturing Systems and Laser Processing (ISI), Joinville, SC, Brazil*

[f] *Department of Mechanical Engineering, Federal University of Santa Catarina (UFSC), Florianópolis, SC, Brazil*

ARTICLE INFO

Article history:
Received 26 August 2020
Accepted 22 December 2020
Available online 31 December 2020

Keywords:
Laser powder bed fusion (LPBF)
Ti–53%Nb (Nb47Ti)
Porosity
Hydride–dehydride (HDH) powder
Cellular microstructure

ABSTRACT

Laser powder bed fusion (LPBF) – also known as selective laser melting (SLM) – is a technology of additive manufacturing (AM) that offers benefits to the fabrication of implants. This approach can create customized and complex parts with low elastic modulus to reduce stress shielding. The use of irregularly shaped powder is not common due to its low flowability and low apparent density. However, its low cost arouses interest in the production of materials by this technology. This work discloses the processing window that allows the fabrication of Ti-53wt.%Nb alloy parts with high density using irregularly shaped powder from hydride–dehydride (HDH) process and analyzes the influence of the process parameters on the microstructure and hardness of the samples manufactured by LPBF. Energy densities (E_V) from 16 to 317 J/mm^3 were investigated. Experimental density measurements by the Archimedes' principle and pore area fraction were calculated and relating to the density estimated based on X-ray diffraction (XRD) results of the HDH powder. Vickers hardness showed strong correlation to the content of interstitial elements of samples made under different E_V. This work proves that is possible to obtain samples with high density using HDH powder in LPBF and that the content of interstitial elements increased with the energy density, as well as the hardness of the alloy.

* Corresponding author.
E-mail address: f.landgraf@usp.br (F.J.G. Landgraf).

https://doi.org/10.1016/j.jmrt.2020.12.084

1. Introduction

Laser powder bed fusion (LPBF) is a technology of additive manufacturing (AM) that uses one or more thermal sources to melt specific areas of powder particles that are spread in the form of layers across the built surface. Once the selected areas of one layer are molten, the build surface is lowered, more powder particles are spread, and new areas are molten. This process is repeated until the part is finished [1]. Detailed reviews of metallic components manufactured by this technology and their defects can be found in [2–5].

The usual feedstock material used in LPBF is spherical shaped powder produced by atomization due to its adequate flowability and apparent density (around 50%) that enable the fabrication of parts with high density [2]. Literature indicates that irregularly shaped powder, such as that fabricated by hydride–dehydride process (HDH), is not adequate to LPBF due to defects caused by inconsistent powder deposition as a consequence of its low flowability and apparent density [2,5–7]. Despite these factors, the lower cost of HDH powders [5,8,9] justifies further investigation of that route. Recently, Narra et al. [10] reported the obtaining of Ti–6Al–4V parts with relative density of 99.8% by electron beam powder bed fusion (EBPBF) from HDH powder after finding the adequate combination of processing parameters.

LPBF has already been used in the medical industry [11]. Currently, Ti–6Al–4V alloy is the most frequently used material in this application due to its high strength and biocompatibility [12,13]. However, aluminum (Al) and vanadium (V) have been claimed potentially cytotoxic. These elements can cause allergic reactions and possible diseases in the human body. There are reports that associate ions of Al and V to long-term health problems as peripheral neuropathy, osteomalacia, and Alzheimer's disease [14–16]. Human exposure to metal derivatives results in a wide range of specific toxicities that can lead to the diseases above and even cancer [17,18]. Another concern in this application is the bone resorption caused by stress shielding when the elastic modulus of the implant is much higher than the elastic modulus of the bone. The stress shielding is one of the most important causes of implant loss [19]. The stiffness mismatch between the bone and implant can be reduced by the insertion of pores in the implant [20–22], by using implant material with low elastic modulus, and/or by the control of its crystalline texture [23,24].

The Ti–53%Nb alloy is highly used in the fabrication of superconducting materials. It may be of interest to the medical industry due to its high biocompatibility and elastic modulus around 80 GPa [25–30]. Although this alloy presents these properties, so far there is only evidence of implant developments with the Ti–42%Nb alloy [31,32]. Moreover, it is known that niobium stabilizes the β phase of body-centered cubic (BCC) structure in the titanium-niobium system and it is possible to retain that phase in a metastable state in the Ti–54%Nb alloy [30,33–36]. The most recent paper about the lattice parameter of β phase for this composition was published by Pattanayak et al. [37], who found a value of 3.285 Å, conforming data of previous literature [33,38–40].

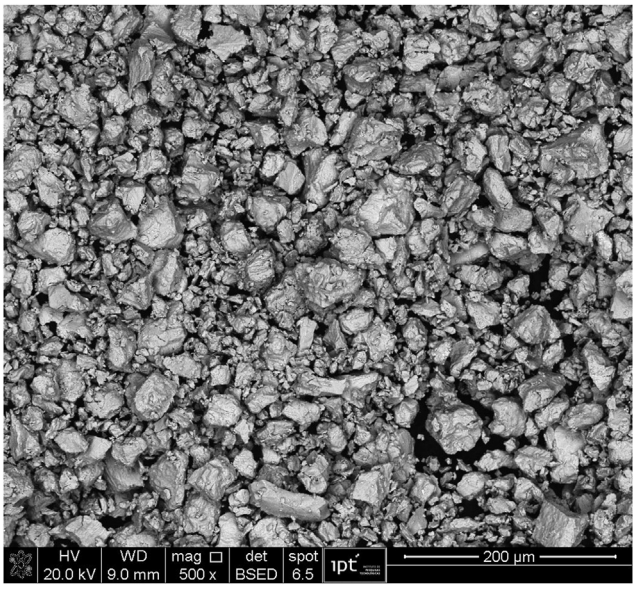

Fig. 1 – Irregular morphology of the powder manufactured by the HDH process (SEM).

In this paper, 10 mm cubes of the Ti–53%Nb alloy were manufactured by LPBF, using HDH powder. Some of them achieving low porosity depending on the power and scanning speed of the laser beam. Two methods were used to measure porosity, pore area fraction by metallography and relative density using the Archimedes' principle and specific mass of the alloy. To find the values of the relative density, the specific mass of the HDH powder was calculated by X-ray diffraction (XRD). Optical microscopy (OM), scanning electron microscopy (SEM), and energy-dispersive X-ray spectroscopy (EDX) were used to analyze and describe the microstructure and defects of the samples with high density. Finally, the hardness of the pieces and their content of interstitial elements were found and related. This work creates a path for the use of the Ti–53%Nb alloy in the fabrication of medical implants, demonstrating that it is possible to obtain material with high density from cheaper HDH powder when compared to the spherical shaped powder by LPBF. More details about that comparison are indicated in the work of Guzmán [41].

2. Experimental procedure

2.1. *Powder characterization*

Irregularly shaped powder was produced by hydride-dehydride process (HDH) from Ti–53%Nb alloy ingots, which were previously obtained by electron beam melting furnace (EBMF) at the Institute for Technological Research (IPT), in São Paulo, Brazil. The ingots of titanium (99.475% purity) and niobium (99.8% purity) were supplied by Acnis do Brasil and the Brazilian Metallurgy and Mining Company (CBMM), respectively. During the hydriding step, the alloy ingots were heated at 650 °C for 3 h, under a constant hydrogen pressure of 1.6 bar, followed by a controlled furnace cooling step. The hydride

alloy ingots were milled in a ring-type mill (Kawasaki Kobe, T-100) and sieved at −53 μm. The dehydriding step of the alloys was carried out under high vacuum at 650 °C for times up to 3 h, followed by a furnace cooling step under high vacuum. More information about similar procedures to those adopted in the obtention of HDH powders of the Ti–53%Nb alloy can be found in the relevant literature [42]. The powder morphology obtained by HDH process is shown in Fig. 1. The HDH powder had a particle size distribution described by Fig. 2, with figures of merit 12 μm (D10), 31 μm (D50), and 67 μm (D90), measured by laser diffraction (Malvern, Mastersizer 2000). The irregularity of the particles was also evaluated by dynamic image analysis (Micromeritics, Particle Insight), showing mean values to circularity and Feret aspect ratio of 0.592 and 1.469, respectively. The circularity is a fractional measure, equal to 1 for a perfect circle. As for Feret aspect ratio, it is defined as the ratio between the Feret length and width, equal to 1 for perfect equiaxial symmetry. This explains the existence, in Fig. 1, of particles with size beyond 100 μm, albeit been screened by 53 μm sieve. The powder presented an apparent density of 1.85 g/cm3 with no flow in hall flowmeter funnel. The oxygen (O), nitrogen (N), and hydrogen (H) contents were determined by inert gas fusion method (LECO, ONH 836) and are listed in Table 1. Density was also measured in a helium gas pycnometer (AccuPyc II 1340).

2.2. Fabrication of the LPBF samples

In this study, 20 samples of Ti–53%Nb alloy in the form of cubes (10 × 10 × 10 mm^3) were fabricated in a Concept Laser M2 printer installed at the SENAI Innovation Institute for Manufacturing Systems and Laser Processing (ISI), in Joinville, Brazil. The displacement of the build platform was chosen as 60 μm to cope with the low flowability and low apparent density of the HDH powder. The spreading of the powder did not present special difficulties, even with the powder having a small fraction of larger particles. It should be taken into account that, with the relative apparent density of 30%, the steady state true layer thickness is 200 μm (platform displacement/relative apparent density) [43]. The recoater

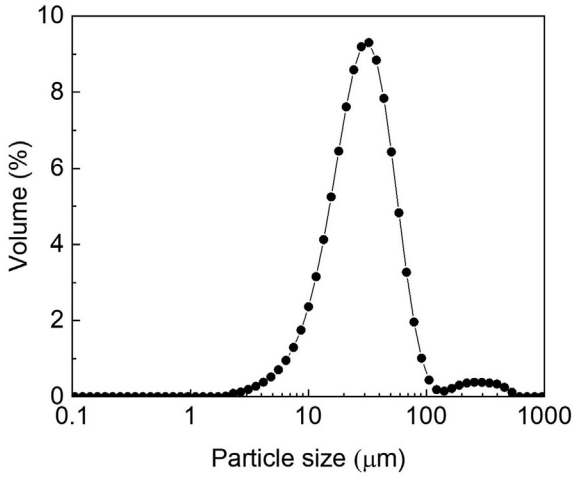

Fig. 2 – Particle size distribution of the Ti–53%Nb HDH powder.

Table 1 – Content of interstitial elements in the HDH powder.

Element	O	N	H
Content (wt.%)	0.34 ± 0.02	0.043 ± 0.005	0.0058 ± 0.003

speed was set at 65 mm/s, the same speed that was used in other experiments with spherical particles. The laser parameters for energy densities from 16 to 317 J/mm^3 are shown in Table 2. The hatch distance was kept constant at 105 μm. As the beam diameter is around 150 μm, the overlapping of melt pools can be estimated as 30%. The energy density (E_V) was calculated using the expression:

$$E_V\left(\frac{J}{mm^3}\right) = \frac{P_L(W)}{V_S\left(\frac{mm}{s}\right)H_S(mm)D_S(mm)}$$

where P_L is laser power, V_S is scanning speed, H_S is hatch distance and D_S is the layer thickness usually assumed in the literature, as the platform displacement [43].

The scanning strategy was a Chessboard tilted 67° relative to one of the walls, with islands of 5 × 5 mm^2. Moreover, a variation of 90° of the laser scanning in each island was used for the subsequent layers as shown in Fig. 3. Furthermore, the process was carried out in a closed chamber continuously flushed with a shielding argon gas to keep the oxygen content to levels between 0.4 and 0.6%.

2.3. Density characterization

Estimates of the relative density were obtained using the Archimedes' principle and pore area fraction. Relative density and porosity are related so that their sum is 100%. The theoretical volumetric mass density was calculated based on the atomic proportion (37%Nb and 63%Ti), the lattice parameter and the niobium (Nb) and titanium (Ti) atomic mass (92.906 and 47.867 g/mol, respectively). To obtain the lattice parameter of the alloy, X-ray diffraction (XRD) was applied to the Ti–53%Nb HDH powder with the extrapolation method of Nelson-Riley [44], as described by the expression:

$$a_{ap} = a_{ext} + b\left(\frac{\cos^2\theta}{\sin\theta} + \frac{\cos^2\theta}{\theta}\right)$$

where a_{ext} is the best estimate of the lattice parameter, based on the extrapolation of the apparent lattice parameter calculated from each θ Bragg angle (a_{ap}). XRD tests were also conducted to check the existence of other phases in the microstructure of the LPBF samples produced with different energy densities. The analyses were done in a Philips-X'Pert PRO PW 3040/00 equipment at 45 kV and 40 mA with a Cu K_α radiation source.

To determine density by the Archimedes' principle, the initially printed cubes were ground with abrasive paper down to 1200 grit and paraffin wax was used to seal surface-connected porosity according to the ASTM standard B962-17 [45]; each sample was measured 3 times. On the other hand, for the pore area fraction method, the samples were polished with a mixture of colloidal silica and hydrogen peroxide until reaching a mirrored surface. Then, 9 micrographs of different zones in planes containing the building direction (BD) at 50×

Table 2 – Process parameters.

Sample	P_L (W)	V_S (mm/s)	E_V (J/mm^3)	Sample	P_L (W)	V_S (mm/s)	E_V (J/mm^3)
1	400	1000	63	11	200	200	159
2	400	800	79	12	200	400	79
3	400	600	106	13	200	600	53
4	400	400	159	14	200	800	40
5	400	200	317	15	200	1000	32
6	300	1000	48	16	100	200	79
7	300	800	60	17	100	400	40
8	300	600	79	18	100	600	26
9	300	400	119	19	100	800	20
10	300	200	238	20	100	1000	16

of magnification were used to measure the relative density using Fiji software [46].

2.4. *Microstructure characterization of the LPBF samples*

The samples with the highest relative density were chosen to have their microstructure and content of interstitial elements analyzed. After samples being polished, they were etched with Kroll's reagent (100 ml of H_2O, 1–3 ml of HF, and 2–6 ml of HNO_3) to reveal their microstructure. Melt pools dimensions of depth and width were measured to observe the influence of the parameters. For this, micrographs were taken in a ZEISS Axio Observer.Z1m microscope and in a field emission gun Inspect 50 Scanning Electron Microscope (FEG-SEM) using secondary electrons (SE) and back-scattered electrons (BSE). Energy-dispersive X-ray spectroscopy (EDX) coupled to the SEM was used for taking chemical composition measurements.

Microhardness was measured in a DuraScan 70 machine using Vickers indentation with a load of 200 g. Each sample was measured on average 10 times in different locations for 15 s. Measurements of O, N, and H were done in samples manufactured with different energy density by inert gas fusion method.

3. Results and discussion

3.1. *X-ray diffraction analysis*

From the X-ray diffractograms shown in Fig. 4, only the diffraction peaks of β phase of BCC structure can be seen in the HDH powder and samples 2 and 10 with energy densities of 79 and 238 J/mm^3, respectively, as expected for this composition according to the literature [33,34,38]. The lattice parameter calculated by Nelson–Riley method approached 3.285 Å, confirming that found by Pattanayak et al. [37] and similar to that found by Baden and Weiss [40], which is the inorganic crystal structure data (ICSD) reference for the Ti–50%Nb composition. Based on that lattice parameter and assuming the composition did not change with processing, theoretical volumetric mass density was estimated as 6.046 g/cm^3. In addition, the density value was also calculated by other methods. First, hydrostatic density (ρ_{Arq}) measurement of the Ti–53%Nb electron beam cast alloy (EBC) resulted in 6.042 g/cm^3. Pycnometer density of the HDH powder resulted in 6.049 ± 0.002 g/cm^3. Among those different estimates and based on the similarity of the lattice parameter found with the other authors [33,37–40], the value of 6.046 g/cm^3 was chosen as the reference specific mass of the alloy to calculate the relative density of the LPBF samples. A recent paper about the Ti–53%Nb published by Mousavi et al. [47] used a density of 6 g/cm^3, a round number that seems not accurate enough for AM applications.

3.2. *Relative density and porosity*

The density of each sample was determined by the Archimedes' principle and pore area fraction method. The relative density was calculated in relation to the reference density value established as the specific mass of the alloy, 6.046 g/cm^3. In Fig. 5, it is possible to see the influence of the variables, P_L and V_S, on the porosity. Samples 1, 2, 6, and 7 successfully

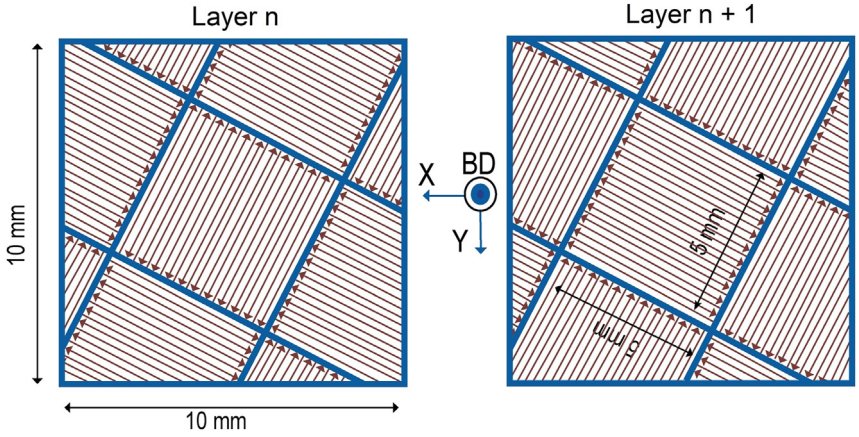

Fig. 3 – Scanning strategy. Layer n: Chessboard tilted 67° with islands of 5 × 5 mm^2. Layer n + 1: the same Chessboard with a variation of 90° of the laser scanning inside each island.

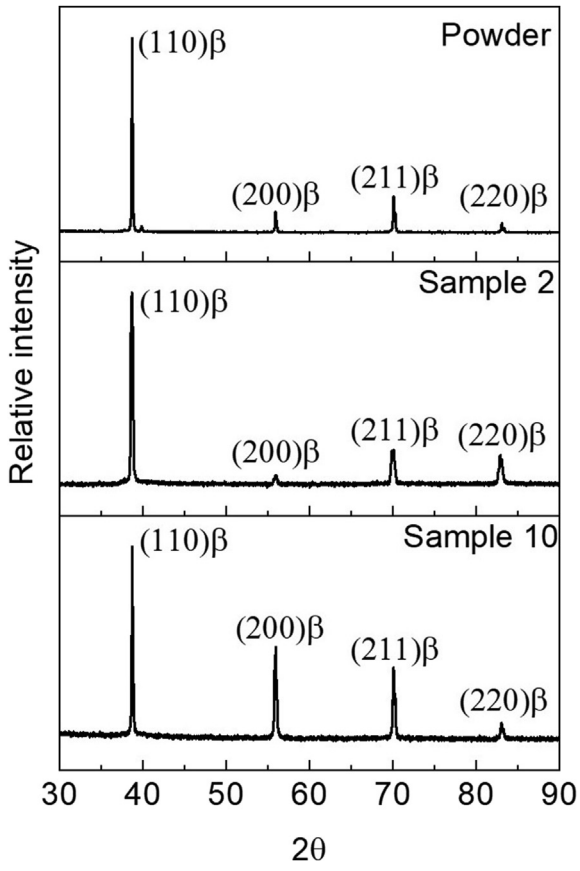

Fig. 4 – Diffractograms of the Ti–53%Nb HDH powder, sample 2 (E_V = 79 J/mm^3) and sample 10 (E_V = 238 J/mm^3) presenting the diffraction peaks of the β phase of BCC structure.

resulted in porosity values below 1%, as measured by both methods. The results by the Archimedes' principle and pore area fraction method differed significantly for samples produced with 100 and 200 W. This is justified because the polishing of samples with high pore area fraction is prone to enlarge the size of the pores. Nevertheless, its use carries special value for revealing the origin of the porosity defects through their morphology, as will be discussed in the microstructural analysis.

The results of relative density obtained by Archimedes' principle as a function of the energy density are presented in Fig. 6. The chart shows that high laser power does not guarantee the highest density. The use of an excessive E_V decreases the density of the pieces and, in some cases, it does not allow the fabrication of samples due to the jamming of the spreading system [48], as it happened in samples 4 (159 J/mm^3) and 5 (317 J/mm^3). Results indicate that Ev is not a good parameter to predict sample density. While an E_V of 159 J/mm^3 to fabricate samples 4 and 11 led only to the fabrication of the latter, the use of an E_V of 79 J/mm^3 for samples 2, 8, 12, and 16 led to cubes with different values of relative density. Porosity depends mainly on power and scanning speed of the laser [5,48–50]. Therefore, it is better to analyze the values of relative density as in Fig. 5 because it presents a broader vision of the processing window used.

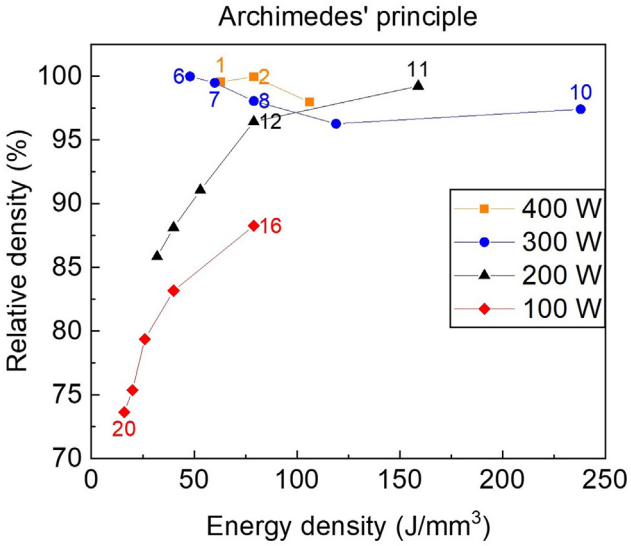

Fig. 6 – Relative density obtained by the Archimedes' principle as a function of energy density.

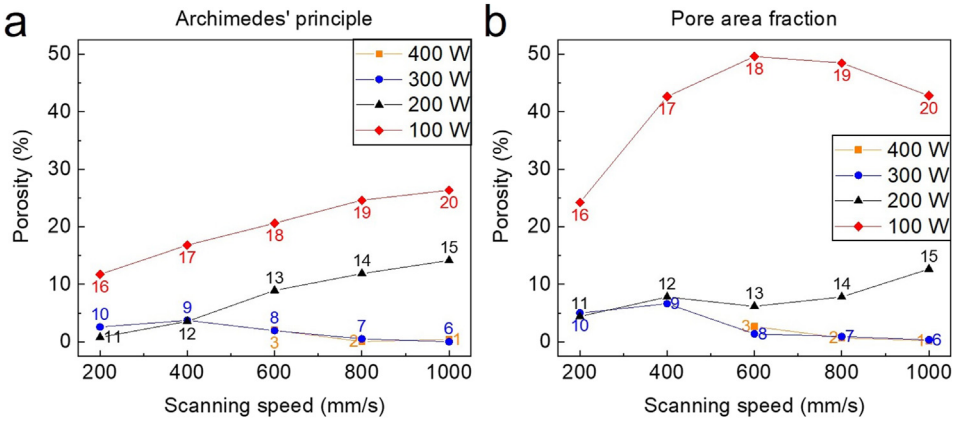

Fig. 5 – Porosity of the LPBF samples. a) Archimedes' principle and b) pore area fraction.

3.3. Microstructural analysis

The LPBF samples were classified according to their defects, using Gong et al. [48] classification in four zones: overheating, incomplete fusion, overmelting, and "fully dense". In this paper, the "fully dense" zone is defined as the power-speed area where samples show porosity below 1% [48]. The micrographs of the samples are organized in a chart in Fig. 7 as a function of power and scanning speed of the laser. The fabrication of samples 4 and 5 had to be interrupted due to damage to the recoater by excessive heating and are classified as the overheating zone. They were manufactured with E_V of 159 and 317 J/mm^3, respectively, and a high P_L of 400 W. The incomplete fusion and overmelting zones can be differentiated by the morphology of pores. In the incomplete melting zone, the porosity has irregular shape from the lack of fusion of some particles due to insufficient energy density [51]. As can be seen for laser power of 100 and 200 W, increasing laser speed led to increasing lack of fusion pores. In the overmelting zone, it is common to have spherical pores produced by trapped gas or vapor [52]. For laser power of 300 and 400 W, decreasing laser speed led to increasing the amount of spherical pores. The "fully dense" zone is formed by samples 1, 2, 6, and 7, produced with P_L from 300 to 400 W and V_S from 800 to 1000 mm/s. They showed a very small amount of pores, originated either from metal vapor, entrapped shielding gas, or even hydrogen from the HDH powder [5,52]. Therefore, that is the processing window to manufacture low porosity LPBF parts of Ti–53%Nb alloy from HDH powder.

Micrographs of the samples with the highest density (1, 2, 6, and 7) are shown in Fig. 8. Their microstructures are composed of melt pools and irregularly shaped grains in a β phase matrix. Melt pool boundaries can be seen due to segregation [53,54]. Moreover, grain boundaries crossing melt pool boundaries can be seen in samples 2 and 6 suggesting epitaxial growth.

It should be noted that the melt pools show different dimensions for each sample. The apparent depth and width of the melt pools are listed in Table 3, after measurements of samples in Fig. 8. The average depth is considerably larger than the platform displacement of 60 μm, while the width is only 20% larger than the hatch distance (105 μm). It was observed that samples fabricated with a P_L of 400 W presented greater depths than samples fabricated with a P_L of 300 W. These results suggest that the melt pool depth increases with P_L, in agreement with other authors [55,56], while the melt pool width does not vary considerably. Samples 1, 2, and 7 present goblet-shaped melt pools, whereas in sample 6 the melt pools show a trend to semicircle shape. In all of them the scanning strategy used resulted in overlapping between melt tracks and consecutive layers.

As expected by the high cooling rate and high temperature gradient in LPBF [2,57,58], all samples presented a cellular structure solidification, as exemplified by SEM images of samples 1 and 6, in Fig. 9. The darker cellular walls in the BSE images (Fig. 9 b, d, and f) indicate that those regions have a higher titanium content, as expected from the Ti–Nb phase diagram [35]. Some authors reported that cellular walls also include dislocation structures [49,57,59]. It is noted that there is a transition from coarse to fine cellular structure from the boundary to the center of the melt pools in all the micrographs, similar to the cell refinement described by Pham et al. [24]. SEM-EDX analyses were performed on the cellular structure in several regions. From the results listed in Table 4 and Fig. 9 for sample 6, it was possible to see that the segregation of Ti was higher at the cell walls. Nevertheless, in some regions of sample 1, it was not possible to find chemical differences between the cell walls and cell interior. This is because the cells are rods with diameters around 1 μm, and that is the dimension of the interaction volume of SEM-EDX

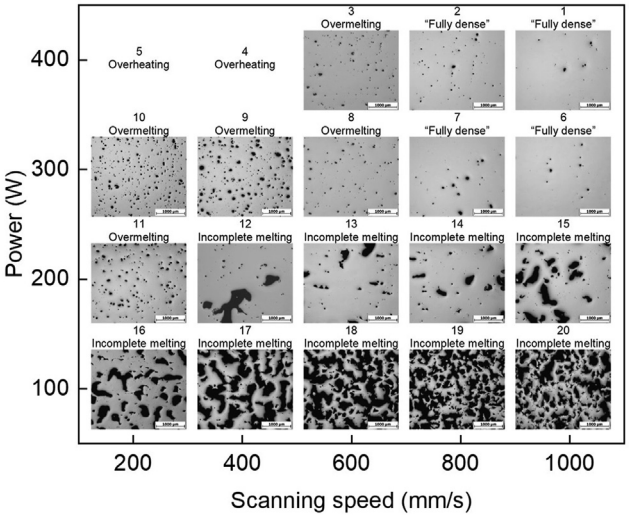

Fig. 7 – Micrographs of the LPBF Ti–53%Nb samples as a function of laser power and scanning speed. The scale bar is 1000 μm and the vertical direction of the OM micrographs is parallel to the building direction.

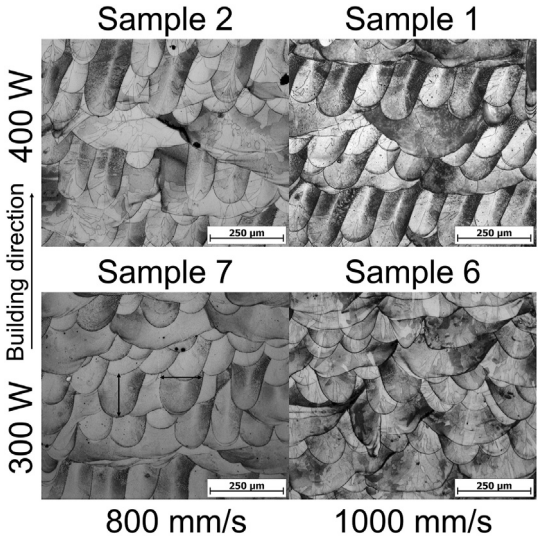

Fig. 8 – Microstructure of the high-density samples. Sample 1 ρ_{Arq} = 99.57%, sample 2 ρ_{Arq} = 99.97%, sample 6 ρ_{Arq} = 99.99%, and sample 7 ρ_{Arq} = 99.46%. Arrows in sample 7 indicate how the apparent melt pool dimensions were measured.

Table 3 – Apparent melt pool dimensions of "fully dense" samples in Fig. 8.

Sample	P_L (W)	V_S (mm/s)	Depth (μm)	Width (μm)
1	400	1000	170 ± 22	125 ± 16
2	400	800	186 ± 31	118 ± 11
6	300	1000	94 ± 25	128 ± 11
7	300	800	147 ± 33	124 ± 13

Table 4 – SEM-EDX analysis results taken in samples 1 and 6 in Fig. 9.

Sample	Position	Accelerating voltage (kV)	Element (wt.%)	
			Ti	Nb
1 (Fig. 9 b)	Cell wall	5.00	46	53
	Cell inner	5.00	46	53
6 (Fig. 9 d)	Cell wall	20.00	54	46
	Cell inner	20.00	48	52
6 (Fig. 9 f)	Cell wall	20.00	52	48
	Cell inner	20.00	50	50

analysis. Therefore, the sensibility of SEM-EDX is limited to perform segregation detection in this kind of samples.

3.4. *Microhardness and interstitial element contents*

The oxygen content of the HDH powder, shown in Table 1, is a major drawback of the HDH process [60]. Nevertheless, as the Ti–53%Nb alloy exhibits a BCC structure, the oxygen content may not impair ductility as much it does in other titanium alloys [61]. Ductility measurements will be presented in a future paper. The LPBF processing in a closed chamber with a shielding atmosphere where oxygen levels were controlled to a maximum of 0.6% led to a further increase in the oxygen and nitrogen content, as shown in Fig. 10 a. The effect of energy density on hardness is presented in Fig. 10 b. Energy density increased the absorption of interstitial elements from the rather high content in the shielding atmosphere. It can be noted that the nitrogen increase was higher than the increase of oxygen content, in relative terms. Although the LPBF process strongly affects the grain size, texture, cellular structure, dislocation density, and segregation [59,62], literature has shown that both, oxygen and nitrogen, harden titanium alloys, being nitrogen the strongest hardener [63,64]. There is a significant increase in hardness, from the ingot (EBC) (160 $HV_{0.2}$) to the LPBF samples, but it must be considered that the oxygen content increased from 0.073 ± 0.001%, in the as cast condition, to 0.34 ± 0.02% in the HDH powder and then to the values shown in Fig. 10 a. The nitrogen content changed from

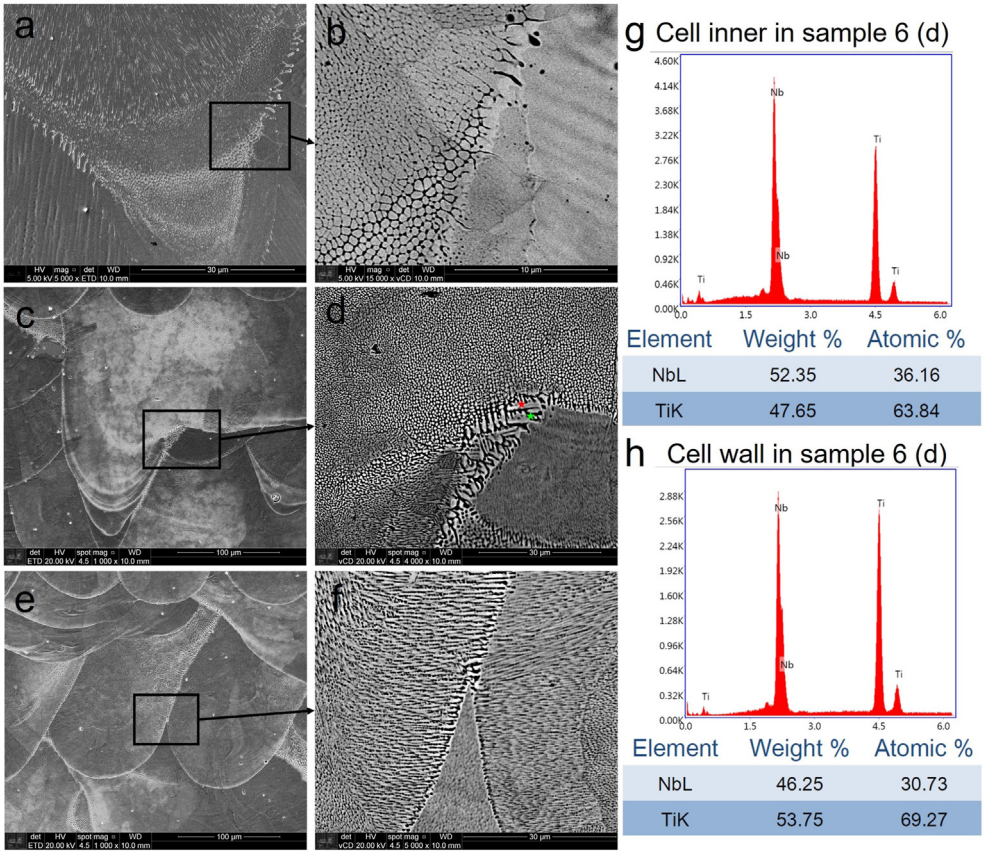

Fig. 9 – Cellular structure in sample 1 and 6. a) and b) Sample 1 (P_L = 400 W and V_S = 1000 mm/s) and c) to f) sample 6 (P_L = 300 W and V_S = 1000 mm/s). a), c) and e) SEM-SE and b), d) and f) SEM-BSE. g) and h) SEM-EDX of sample 6 in red and green points in d). (For interpretation of the references to color in this figure legend, the reader is referred to the Web version of this article.)

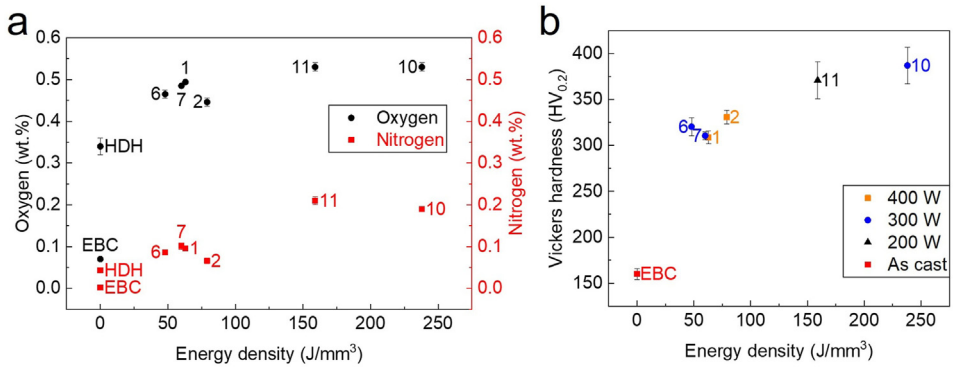

Fig. 10 – Effect of energy density on a) oxygen and nitrogen contents and b) Vickers hardness of the samples.

0.002 ± 0.001% to 0.043 ± 0.005% and to 0.2 ± 0.01%, respectively. Therefore, the increase in the hardness of the LPBF samples can be attributed to the absorption of interstitial atoms, that are solid solution strengtheners. The content of hydrogen increased with respect to the initial powder (0.0058 ± 0.003 wt.%) and kept stable after reaching 0.02% for all the manufactured samples. It needs to be said, that the content of H was very low when compared with the contents of O and N reached by the LPBF samples, for that reason, H is not presented in Fig. 10 a.

These results show that if high laser power needs to be used, a reduction in the levels of oxygen in the closed chamber is necessary. Therefore, further studies are needed to reduce the oxygen content in the closed chamber aiming at lowering the hardness of the LPBF Ti–53%Nb alloy from HDH powder with processing parameters outside from the overheating zone. These analyses can be performed using more combinations of power and scanning speed of the laser inside the "fully dense" zone found in order to obtain specific microstructures (different melt pool and grain shapes).

4. Conclusions

Parts of Ti–53%Nb alloy from irregularly shaped hydride-dehydride (HDH) powder were manufactured by laser powder bed fusion (LPBF) to find a high-density processing window. The conclusions can be summarized as follows:

- It was possible to obtain samples with relative density higher than 99%, assuming a volumetric mass density of 6.046 g/cm^3 determined from a lattice parameter of 3.285 Å for the Ti–53%Nb alloy. The high-density process window was found in the laser power interval of 300–400 W and scanning speeds higher than 800 mm/s.
- The final oxygen content is near 0.5%, as the HDH powder had an oxygen content of 0.34%, and the chamber atmosphere oxygen content was kept only below 0.6%. Further studies in the processing parameter range to avoid overheating and absorption of interstitial elements are necessary.
- The microstructure composed by β phase of BCC structure presented irregularly shaped grains, cellular structure with segregation of Ti at the cell walls, and different melt pool forms. Moreover, the oxygen content in the samples with high relative density, below 0.5%, did not affect the microstructure. However, it is recommended to decrease it for medical applications.
- Samples manufactured with high energy density were more likely to absorb oxygen, and their hardness was affected by the content of interstitial elements in the samples. The values varied from 309 to 387 $HV_{0.2}$.

Data availability statement

All data reported in this paper is contained within the manuscript.

Declaration of Competing Interest

The authors declare that they have no conflict of interest.

Acknowledgment

The authors would like to express their gratitude to the São Paulo Research Foundation (FAPESP) (process number 2016/50199-6), the Brazilian Metallurgy and Mining Company (CBMM), the Disabled Child Care Association (AACD), and the Brazilian Agency for Industrial Research and Innovation (EMBRAPII) for their financial support. R.B. Falcão (Grant no. 2017/20926-6) and Edwin Sallica-Leva (Grant no. 2017/20877-5) gratefully acknowledge FAPESP for providing postdoctoral fellowships. F.J.G. Landgraf acknowledges CNPq support to project 307631/2018-4. Thanks must also be given to S.D. Brandi and G.F.B. Lenz e Silva for their collaboration in the hardness and hydrostatic density tests.

REFERENCES

[1] Gibson I, Rosen D, Stucker B. Additive manufacturing technologies. 2nd. ed. New York: Springer; 2015. p. 107–45. Chapter 5, Powder Bed Fusion Processes.

[2] DebRoy T, Wei HL, Zuback JS, Mukherjee T, Elmer JW, JO Milewski, et al. Additive manufacturing of metallic components – process, structure and properties. Prog Mater Sci 2018;92:112–224. https://doi.org/10.1016/j.pmatsci.2017.10.001.
[3] Herzog D, Seyda V, Wycisk E, Emmelmann C. Additive manufacturing of metals. Acta Mater 2016;117:371–92. https://doi.org/10.1016/j.actamat.2016.07.019.
[4] Murr LE, Martinez E, Amato KN, Gaytan SM, Hernandez J, Ramirez DA, et al. Fabrication of metal and alloy components by additive manufacturing: examples of 3D materials science. J Mater Res Technol 2012;1:42–54. https://doi.org/10.1016/S2238-7854(12)70009-1.
[5] Sames WJ, List FA, Pannala S, Dehoff RR, Babu SS. The metallurgy and processing science of metal additive manufacturing. Int Mater Rev 2016;61:315–60. https://doi.org/10.1080/09506608.2015.1116649.
[6] Spierings AB, Voegtlin M, Bauer T, Wegener K. Powder flowability characterisation methodology for powder-bed-based metal additive manufacturing. Prog Addit Manuf 2016;1:9–20. https://doi.org/10.1007/s40964-015-0001-4.
[7] Kurzynowski T, Chlebus E, Kuźnicka B, Reiner J. Parameters in selective laser melting for processing metallic powders. In: Proc. SPIE 8239, high power laser materials processing: lasers, beam delivery, diagnostics, and applications; 2012. p. 823914. https://doi.org/10.1117/12.907292. San Francisco, California, United States.
[8] Ivasishin O, Moxson V. Titanium powder metallurgy. 1st. ed. Elsevier; 2015. p. 117–48. https://doi.org/10.1016/B978-0-12-800054-0.00008-3. Chapter 8, Low-cost titanium hydride powder metallurgy.
[9] Xu W, Xiao S, Lu X, Chen G, Liu C, Qu X. Fabrication of commercial pure Ti by selective laser melting using hydride-dehydride titanium powders treated by ball milling. J Mater Sci Technol 2019;35:322–7. https://doi.org/10.1016/j.jmst.2018.09.058.
[10] Narra SP, Wu Z, Patel R, Capone J, Paliwal M, Beuth J, et al. Use of non-spherical hydride-dehydride (HDH) powder in powder bed fusion additive manufacturing. Addit Manuf 2020;34:101188. https://doi.org/10.1016/j.addma.2020.101188.
[11] Murr LE. Metallurgy principles applied to powder bed fusion 3D printing/additive manufacturing of personalized and optimized metal and alloy biomedical implants: an overview. J Mater Res Technol 2020;9:1087–103. https://doi.org/10.1016/j.jmrt.2019.12.015.
[12] Liu S, Shin YC. Additive manufacturing of Ti6Al4V alloy: a review. Mater Des 2019;164:107552. https://doi.org/10.1016/j.matdes.2018.107552.
[13] Geetha M, Singh AK, Asokamani R, Gogia AK. Ti based biomaterials, the ultimate choice for orthopaedic implants – a review. Prog Mater Sci 2009;54:397–425. https://doi.org/10.1016/j.pmatsci.2008.06.004.
[14] Rao S, Ushida T, Tateishi T, Okazaki Y, Asao S. Effect of Ti, Al, and V ions on the relative growth rate of fibroblasts (L929) and osteoblasts (MC3T3-E1) cells. Bio Med Mater Eng 1996;6:79–86.
[15] Walker PR, LeBlanc J, Sikorska M. Effects of aluminum and other cations on the structure of brain and liver chromatin. Biochemistry 1989;28:3911–5.
[16] Lin C-W, Ju C-P, Chern Lin J-H. A comparison of the fatigue behavior of cast Ti–7.5Mo with c.p. titanium, Ti–6Al–4V and Ti–13Nb–13Zr alloys. Biomaterials 2005;26:2899–907. https://doi.org/10.1016/j.biomaterials.2004.09.007.
[17] Guillamet E, Creus A, Farina M, Sabbioni E, Fortaner S, Marcos R. DNA-damage induction by eight metal compounds in TK6 human lymphoblastoid cells: results obtained with the alkaline Comet assay. Mutat Res Toxicol Environ Mutagen 2008;654:22–8. https://doi.org/10.1016/j.mrgentox.2008.04.005.
[18] Gomes CC, Moreira LM, Santos VJSV, Ramos AS, Lyon JP, Soares CP, et al. Assessment of the genetic risks of a metallic alloy used in medical implants. Genet Mol Biol 2011;34:116–21. https://doi.org/10.1590/S1415-47572010005000118.
[19] Ridzwan MIZ, Shuib S, Hassan AY, Shokri AA, Ibrahim MNM. Problem of stress shielding and improvement to the hip implant designs: a review. J Med Sci 2007;7:460–7. https://doi.org/10.3923/jms.2007.460.467.
[20] Luo JP, Huang YJ, Xu JY, Sun JF, Dargusch MS, Hou CH, et al. Additively manufactured biomedical Ti-Nb-Ta-Zr lattices with tunable Young's modulus: mechanical property, biocompatibility, and proteomics analysis. Mater Sci Eng C 2020;114:110903. https://doi.org/10.1016/j.msec.2020.110903.
[21] Hafeez N, Liu J, Wang L, Wei D, Tang Y, Lu W, et al. Superelastic response of low-modulus porous beta-type Ti-35Nb-2Ta-3Zr alloy fabricated by laser powder bed fusion. Addit Manuf 2020;34:101264. https://doi.org/10.1016/j.addma.2020.101264.
[22] Attar H, Ehtemam-Haghighi S, Soro N, Kent D, Dargusch MS. Additive manufacturing of low-cost porous titanium-based composites for biomedical applications: advantages, challenges and opinion for future development. J Alloys Compd 2020;827:154263. https://doi.org/10.1016/j.jallcom.2020.154263.
[23] Sun Z, Tan X, Tor SB, Chua CK. Simultaneously enhanced strength and ductility for 3D-printed stainless steel 316L by selective laser melting. NPG Asia Mater 2018;10:127–36. https://doi.org/10.1038/s41427-018-0018-5.
[24] Pham M-S, Dovgyy B, Hooper PA, Gourlay CM, Piglione A. The role of side-branching in microstructure development in laser powder-bed fusion. Nat Commun 2020;11:749. https://doi.org/10.1038/s41467-020-14453-3.
[25] Cooley Lee, Larbalestier. Flux-pinning mechanism of proximity-coupled planar defects in conventional superconductors: evidence that magnetic pinning is the dominant pinning mechanism in niobium-titanium alloy. Phys Rev B Condens Matter 1996;53:6638–52.
[26] Zhuravleva K, Scudino S, Khoshkhoo MS, Gebert A, Calin M, Schultz L, et al. Mechanical alloying of β-type Ti-Nb for biomedical applications. Adv Eng Mater 2013;15:262–8. https://doi.org/10.1002/adem.201200117.
[27] Olesova VN, Shashmurina VR, Shugailov IA, Olesov EE, Mirgazizov MZ. Study of the biocompatibility of titanium-niobium implants by the parameters of their osseointegration under experimental conditions. Bull Exp Biol Med 2019;166:686–8. https://doi.org/10.1007/s10517-019-04418-y.
[28] Godley R, Starosvetsky D, Gotman I. Corrosion behavior of a low modulus β-Ti-45%Nb alloy for use in medical implants. J Mater Sci Mater Med 2006;17:63–7. https://doi.org/10.1007/s10856-006-6330-6.
[29] Ozaki T, Matsumoto H, Watanabe S, Hanada S. Beta Ti alloys with low Young's modulus. Mater Trans 2004;45:2776–9. https://doi.org/10.2320/matertrans.45.2776.
[30] Hon Y-H, Wang J-Y, Pan Y-N. Composition/phase structure and properties of titanium-niobium alloys. Mater Trans 2003;44:2384–90. https://doi.org/10.2320/matertrans.44.2384.
[31] Schulze C, Weinmann M, Schweigel C, Keßler O, Bader R. Mechanical properties of a newly additive manufactured implant material based on Ti-42Nb. Materials 2018;11:124. https://doi.org/10.3390/ma11010124.
[32] Huang S, Sing SL, Yeong WY. Selective laser melting of Ti42Nb composite powder and the effect of laser Re-melting. Key Eng Mater 2019;801:270–5. https://doi.org/10.4028/www.scientific.net/kem.801.270.

[33] Murray JL. The Nb–Ti (Niobium-Titanium) system. Bull Alloy Phase Diagrams 1981;2:55–61. https://doi.org/10.1007/BF02873704.
[34] Lee CM, Ju CP, Chern Lin JH. Structure-property relationship of cast Ti-Nb alloys. J Oral Rehabil 2002;29:314–22.
[35] Moffat DL, Kattner UR. The stable and metastable Ti-Nb phase diagrams. Metall Trans A 1988;19:2389–97. https://doi.org/10.1007/BF02645466.
[36] Ahmed T, Rack HJ. Martensitic transformations in Ti-(16–26 at%) Nb alloys. J Mater Sci 1996;31:4267–76. https://doi.org/10.1007/BF00356449.
[37] Pattanayak D, Obst B, Wolfstieg U. X-ray phase determination in niobium-titanium superconductors. Zeitschrift fuer Metallkunde 1981;72(7):481–6.
[38] Hansen M, Kamen EL, Kessler HD, McPherson DJ. Systems titanium-molybdenum and titanium-columbium. JOM 1951;3:881–8. https://doi.org/10.1007/BF03397396.
[39] Rudy E. Ternary phase equilibria in transition metal-boron-carbon-silicon systems. Sacramento, Calif: Aerojet-General Corp.; 1969. Materials Research Lab. AFML-TR-65-2(Pt.5).
[40] Baden W, Weiss A. X-ray and 1H-NMR studies on niobium-titanium-hydrides. Zeitschrift fuer Metallkunde 1983;74(2):89–93.
[41] Guzmán Hernández JS. Microstructural and mechanical analyses of Ti-53%Nb alloy manufactured by selective laser melting using spherical and irregular powders [M.Sc. dissertation]. São Paulo: Polytechnic School of the University of São Paulo; 2020. https://doi.org/10.11606/D.3.2020.tde-21042020-100214.
[42] Falcão RB, Sallica-Leva E, Bayerlein DL, Neto JBF, Landgraf FJG. Obtention of Nb47Ti and Ti13Nb13Zr alloys powders by hydride-dehydride process for additive manufacturing applications. Mater Sci Forum 2020;1012:343–8. https://doi.org/10.4028/www.scientific.net/MSF.1012.343.
[43] Mindt HW, Megahed M, Lavery NP, Holmes MA, Brown SGR. Powder bed layer characteristics: the overseen first-order process input. Metall Mater Trans A 2016;47:3811–22. https://doi.org/10.1007/s11661-016-3470-2.
[44] Nelson JB, Riley DP. An experimental investigation of extrapolation methods in the derivation of accurate unit-cell dimensions of crystals. Proc Phys Soc 1945;57:160–77. https://doi.org/10.1088/0959-5309/57/3/302.
[45] ASTM International. ASTM B962-17, standard test methods for density of compacted or sintered powder Metallurgy (PM) products using Archimedes' principle. 2017. https://doi.org/10.1520/B0962-17.
[46] Schindelin J, Arganda-Carreras I, Frise E, Kaynig V, Longair M, Pietzsch T, et al. Fiji: an open-source platform for biological-image analysis. Nat Methods 2012;9:676–82. https://doi.org/10.1038/nmeth.2019.
[47] Mousavi T, Hong Z, Morrison A, London A, Grant PS, Grovenor C, et al. A new approach to fabricate superconducting NbTi alloys. Supercond Sci Technol 2017;30:094001. https://doi.org/10.1088/1361-6668/aa793d.
[48] Gong H, Rafi K, Gu H, Starr T, Stucker B. Analysis of defect generation in Ti–6Al–4V parts made using powder bed fusion additive manufacturing processes. Addit Manuf 2014;1–4:87–98. https://doi.org/10.1016/j.addma.2014.08.002.
[49] Qiu C, Kindi M Al, Aladawi AS, Hatmi I Al. A comprehensive study on microstructure and tensile behaviour of a selectively laser melted stainless steel. Sci Rep 2018;8:7785. https://doi.org/10.1038/s41598-018-26136-7.
[50] Miranda G, Faria S, Bartolomeu F, Pinto E, Madeira S, Mateus A, et al. Predictive models for physical and mechanical properties of 316L stainless steel produced by selective laser melting. Mater Sci Eng A 2016;657:43–56. https://doi.org/10.1016/j.msea.2016.01.028.
[51] Khairallah SA, Anderson AT, Rubenchik A, King WE. Laser powder-bed fusion additive manufacturing: physics of complex melt flow and formation mechanisms of pores, spatter, and denudation zones. Acta Mater 2016;108:36–45. https://doi.org/10.1016/j.actamat.2016.02.014.
[52] Martin AA, Calta NP, Khairallah SA, Wang J, Depond PJ, Fong AY, et al. Dynamics of pore formation during laser powder bed fusion additive manufacturing. Nat Commun 2019;10:1987. https://doi.org/10.1038/s41467-019-10009-2.
[53] Davies GJ, Garland JG. Solidification structures and properties of fusion welds. Int Metall Rev 1975;20(1):83–108. https://doi.org/10.1179/imtlr.1975.20.1.83.
[54] Xiong ZH, Liu SL, Li SF, Shi Y, Yang YF, Misra RDK. Role of melt pool boundary condition in determining the mechanical properties of selective laser melting AlSi10Mg alloy. Mater Sci Eng A 2019;740–741:148–56. https://doi.org/10.1016/j.msea.2018.10.083.
[55] Qi T, Zhu H, Zhang H, Yin J, Ke L, Zeng X. Selective laser melting of Al7050 powder: melting mode transition and comparison of the characteristics between the keyhole and conduction mode. Mater Des 2017;135:257–66. https://doi.org/10.1016/j.matdes.2017.09.014.
[56] Chen ZW, Guraya T, Darvish K, Phan MAL, Pasang T. Solidification during selective laser melting of Co-29Cr-6Mo alloy. JOM 2019;71:691–6. https://doi.org/10.1007/s11837-018-3264-7.
[57] Chalmers B. Principles of solidification. 1st ed. Wiley; 1964.
[58] Liu L, Ding Q, Zhong Y, Zou J, Wu J, Chiu Y-L, et al. Dislocation network in additive manufactured steel breaks strength–ductility trade-off. Mater Today 2018;21:354–61. https://doi.org/10.1016/j.mattod.2017.11.004.
[59] Wang YM, Voisin T, McKeown JT, Ye J, Calta NP, Li Z, et al. Additively manufactured hierarchical stainless steels with high strength and ductility. Nat Mater 2017;17:63–71. https://doi.org/10.1038/nmat5021.
[60] McCracken CG, Barbis DP, Deeter RC. Key characteristics of hydride–dehydride titanium powder. Powder Metall 2011;54:180–3. https://doi.org/10.1179/174329011X13045076771849.
[61] Jablokov VR, Freese HL. Titanium alloys including increased oxygen content and exhibiting improved mechanical properties. 2007. US20070193662A1.
[62] Liu C, Zhang M, Chen C. Effect of laser processing parameters on porosity, microstructure and mechanical properties of porous Mg-Ca alloys produced by laser additive manufacturing. Mater Sci Eng A 2017;703:359–71. https://doi.org/10.1016/j.msea.2017.07.031.
[63] Ogden HR, Jaffee RI. The effects of carbon, oxygen, and nitrogen on the mechanical properties of titanium and titanium alloys. Columbus, Ohio: Battelle Memorial Inst. Titanium Metallurgical Lab.; 1955. https://doi.org/10.2172/4370612. TML-20.
[64] Conrad H. Effect of interstitial solutes on the strength and ductility of titanium. Prog Mater Sci 1981;26:123–403. https://doi.org/10.1016/0079-6425(81)90001-3.